VORTEX-INDUCED VIBRATION OF MARINE CABLES: EXPERIMENTS USING FORCE FEEDBACK

F. S. Hover, S. N. Miller and M. S. Triantafyllou
Department of Ocean Engineering, Massachusetts Institute of Technology
Cambridge, MA 02139, U.S.A.

The problem of vortex-induced vibrations in flexibly mounted cylinders and marine cables is addressed using a new laboratory apparatus, which combines force-feedback with on-line numerical simulation of a modeled structure. We establish correlation with published single-mode, free vibration data, and give results for a dynamic model having the principal characteristics of inclined cables, i.e. pairs of weakly coupled modes and crossover avoidance. While the fluid lift properties of the single-mode and multiple-mode systems are qualitatively similar, the spectra differ in several fundamental ways, suggesting distinct wake interaction processes.

©1997 Academic Press Limited

1. INTRODUCTION

VORTEX-INDUCED VIBRATIONS (VIV) of cables and pipes are ubiquitous during ocean towing, and in marine applications involving free spans subjected to ambient currents. These vibrations are of significant engineering importance because a compliant member can develop an increased drag coefficient, which alters the static configuration, and thereby increases the static loading (Every *et al.* 1981; Sarpkaya 1978; Yoerger *et al.* 1991). Furthermore, these excitations can lead to large dynamic loads at the forcing frequency, reducing the system's fatigue life.

Full-scale studies reveal that the vibrations are characterized by a spectrum containing several frequencies, often dominated by strong beating oscillations (Alexander 1981; Grosenbaugh *et al.* 1991; Vandiver & Chung 1987). One cause is current shear; the vortex-shedding rate has a roughly linear dependence on local velocity even for short cylinder spans placed in a nonuniform flow (Stansby 1976). Nearly all deployments involve shear of some sort, while curved cables are also subject to a spatially varying normal velocity, even within a uniform current. The variation in normal oncoming velocity can be shown analytically to lead to beating-type behavior in long members (Howell 1989). Additionally, cables with significant in-water weight and normal drag forces are subject to sagging, and as such possess a nonuniform multi-mode dynamic response (Irvine & Caughey 1974; Triantafyllou 1984).

We have developed a force-feedback laboratory apparatus which allows modeling of complex structural dynamics, while fully accounting for fluid–structure interaction. The experiments described in this paper represent a fundamental divergence from VIV studies to date, and a short review of past work helps to illuminate the differences. A great number of researchers have performed laboratory work with test cylinders, either fixed or motor-driven (Bishop & Hassan 1964; Protos *et al.* 1968; Mercier 1973; Sarpkaya 1978; Staubli 1983; Schargel 1980; Gopalkrishnan 1992). Forced-motion tests, employing sinusoidal or beating motions, achieve the gross features of observed VIV phenomena, although the essence of fluid–structure interaction is missing; that is, no

matching exists between the dynamics of the structure and the wake. Free-vibration tests, such as initiated by Feng (1968) (in air), Anand (1985), and Moe & Wu (1989), allow the complete coupled process to develop, although only relatively simple, single-mode mass-spring systems have been used. Free vibrations of flexibly mounted, rigid cylinder sections with multi-mode responses have not been considered experimentally. However, progress in understanding multi-mode responses has been made by Nakano & Rockwell (1993) and Gopalkrishnan (1992), who studied forced beating oscillations. In addition, nonlinear compliant systems have not been studied experimentally; the nonlinearities arise from geometric (typically quadratic or cubic), or material properties.

In Section 2, we describe how the present apparatus employs a hybrid experimental and numerical simulation approach: structural vibrations are simulated in software, using as excitation the real-time force measurements from a load cell attached to a test cylinder. This cylinder is a physical component of the modeled structure and, when placed within an on-coming steady flow, oscillates transversely with the motion predicted by the numerical simulation, using a computer-controlled servo motor. The result is a closed-loop system that simulates the overall fluid–structure interaction process. It should be noted that the two ends of our test cylinder move together, and that no in-line oscillations take place.

In the subsequent sections, we first study the applicability of our approach to single-mode compliance, computing lift force amplitude and phase, as well as power spectra. Then we investigate bimodal structural dynamics in the context of a low-ordered inclined cable model, whose response is characterized by pairs of closely spaced eigenvalues and weakly coupled modes. Specifically, what we wish to study here is the qualitative fluid–structure interaction when avoided crossings, and hence large sensitivity to parametric changes, are exhibited by the structure.

In this paper, we chose to couple the model of the extended cable structure with a short span wake, since the latter can be adequately represented by our experimental facility. Outside the test cylinder, we did not wish to obscure the basic problem by having to assume models for the hydrodynamic loading, such as correlation length. Thus, although the structural dynamic response includes the entire cable, fluid forcing is applied only at the location of the test cylinder. We recognize that the hybrid test apparatus is a simplification, and that most often in practice cables are exposed along their whole span to fluid forcing. The inclined cable problem is a natural setting for this work, but the new phenomena we report pertain strictly to multi-mode compliance. Notation is given in the Appendix.

2. APPARATUS

2.1. HARDWARE

At the MIT Testing Tank Facility, a moving carriage has been outfitted with a micro-computer, servomotor system, lead-screw assembly, and a yoke with a cylindrical test section; see Figure 1. This apparatus is an adaptation of that used by Gopalkrishnan (1992). The tank is 1·4 m deep and 2·6 m wide, with a working length of 18 m. The test cylinder is mounted on a piezoelectric quartz load cell, and we measure the location of the yoke with a linear variable differential transformer (LVDT). The test cylinder is 62 cm long, with a diameter of 3·175 cm, and has circular end-plates of 35 cm diameter. We used carriage speeds of 0·23–0·36 m/s in the tests, for a Reynolds number range of
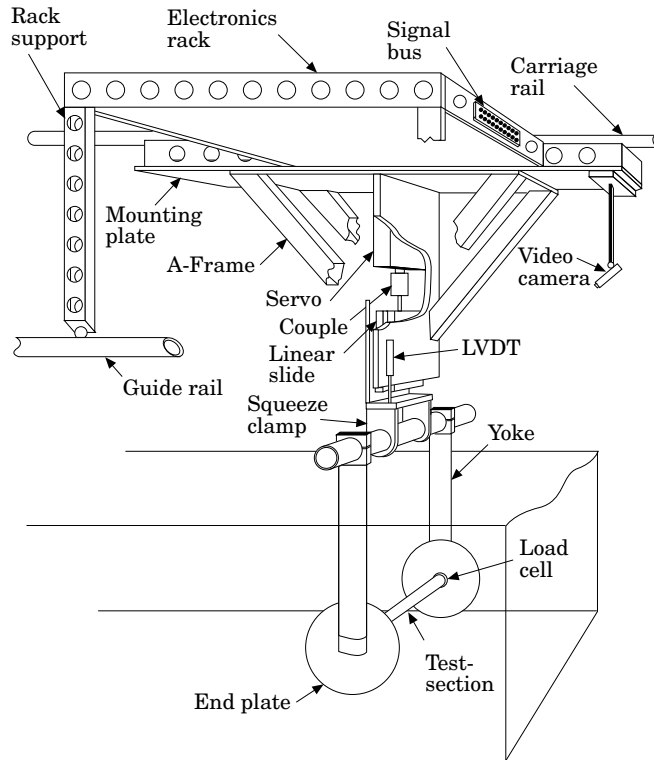
Figure 1. A computer-controlled servomotor actively positions the test cylinder through a linear slide; this assembly, along with the supporting electronics and sensors, translates along a 25 m towing tank.

7200–11 500. These values are typical for metallic mooring or towing lines operating in slow to moderate ocean currents.

As shown in Figure 2, the force feedback loop uses measured forces on the test cylinder to drive a real-time simulation of the physical cable system; the output of the simulation then provides the motor setpoint. Ideally, the simulator has an exact dynamic response, albeit subject to some amount of noise and filtering effects. The 950-Watt DC motor is controlled by a digital servo loop closed at 12 khz, and the peak force output through the linear drive is 6 000 N, which compares favorably with fluid forces on the order of 5 N and inertial loads on the order of 2 400 N. A number of steps were taken to ensure clean measurements and smooth operation. First, we stiffened the carriage lower assembly, and used rubber wheels with durometer hardness 60–70 to
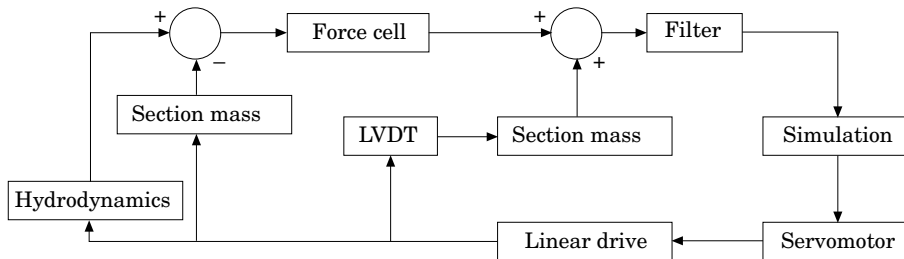
Figure 2. Force-feedback with an inertial correction enables real-time dynamic.

isolate the force sensor from irregularities on the carriage rail. In order to minimize electromagnetic noise, all connections and wiring were shielded; we placed the control and simulation computer on the carriage itself. Finally, we tuned the motor servo so that less than 1 deg. of phase could be discerned, for oscillations of 3 cm amplitude and frequency 15 rad/s. With respect to other hardware, the lead-screw has a specified backlash of 5 μm. Measurement of the carriage speed indicated a worst-case error of 2%; several seconds of data during the carriage acceleration and oscillation growth were truncated at the beginning of each run. To maximize the useful data length, we initialized each run with 3 s of stored simulation states and physical oscillations from a previous run. Variances for the force sensor and the LVDT were computed as $9 \times 10^{-4}\,\mathrm{N}^2$, and $4 \times 10^{-4}\,\mathrm{cm}^2$, respectively.

2.2. Programming and Processing

The transverse force data were corrected on-line for the inertia of the apparatus. To illustrate, in the case of the linear mass-spring-dashpot models, the desired behavior is governed by the equation

$$m\ddot{y}(t) + b\dot{y}(t) + ky = F(t),   \tag{1}$$

where $F(t)$ is purely fluid forcing.† However, the measured force, $F_m(t)$, is actually

$$F_m(t) = F(t) - m_{\mathrm{cyl}}\ddot{y}(t),   \tag{2}$$

where m_{cyl} is the actual mass of the test cylinder, plus some small entrained water mass around the force sensor. Therefore, to retain the desired dynamics, the governing equation becomes

$$m\ddot{y}(t) + b\dot{y}(t) + ky(t) = F_m(t) + m_{\mathrm{cyl}}\ddot{y}(t).   \tag{3}$$

With the right-side of this equation representing the force seen by the numerical model, we discretized the dynamic equation using the matrix exponential. The control loop bandwidth is 500 Hz, well above that required to track the 3 Hz oscillations of interest. One important and typical assumption is that of the zero-order hold, i.e., that $F(t)$ is held constant between samples. This yields the following linear discrete-time system, to be applied at each time step in the simulation:

$$\mathbf{x}(t + \Delta t) = \Phi\bar{\mathbf{x}}(t) + \Gamma F(t).   \tag{4}$$

In the single-mode case, $\mathbf{x}(t)$ consists of cylinder velocity and position, while Φ and Γ are 2×2 and 2×1 constant matrices, respectively. The position or velocity can thus pass directly to the servomotor at each time step. Note that since the simulation runs at 500 Hz, while the servomotor samples the setpoint at 12 kHz, a second zero-order hold approximation exists.

  Because the cylinder used for the tests is quite heavy (density 1500 kg/m³), we encountered some chatter in the closed-loop from the large inertial correction. Part of this is certainly due to double differentiation of the LVDT signal, but a similar, more general problem exists for robotic arms interacting with massive or rigid environments. Specifically, a nonyielding surface that is normal to the motion naturally prohibits position control in this direction (Mason 1981), and in most practical cases the robot must be programmed to be suitably compliant. In contrast, our experimental technique insists upon position control, with the cylinder mass acting as the nonyielding

---

† In the case of a distributed cable, we use $F(s, t)$ to indicate forcing dependence on location as well as time.

environment. To our knowledge, no general solution exists in this application except for low-pass filtering; we employed a Chebyshev third-order digital filter with cutoff at 100 rad/s. This filter brings a lag of about 12 deg. at the fixed-cylinder vortex-shedding rate, but achieves very smooth motion. We believe that the overall effect of this lag is minor, as evidenced by the data in later sections. A similar phase loss also applies to the inclined-cable results of this paper; we are presently developing a much lighter cylinder for future tests. With the inertial correction and filter in place, we verified proper static deflections, natural frequencies, and decay envelopes for the feedback system in air.

Linear vertical position, horizontal force (not presented), and vertical force were recorded on a separate, dedicated computer at 100 Hz. During processing, we looked only at regions of fully developed beating. For computing the spectra, we detrended and employed a Hanning window. We obtained displacement magnitudes by finding the peaks between zero crossings, and averaging the top 10%.

2.3. DEFINITIONS

The experiments are parameterized with the ratio of the damped structural frequency to the fixed-cylinder vortex-shedding rate:

$$\omega_t = \frac{\omega_d}{\omega_S} = \frac{5 \cdot 25}{V_r}, \tag{5}$$

where V_r is the standard reduced velocity $2\pi U / \omega_d d$, and $S = 0 \cdot 19$. In the single-mode cases, we also varied the damping ratio ζ.

In sinusoidal forced vibration tests, fluid forcing can be decomposed into a lift component in phase with the lateral velocity, C_{Fv}, and an added mass component in phase with the acceleration, C_{Fa}. The lift force is nondimensionalized with dynamic pressure:

$$C_{Fv} = \frac{F_0 \sin \psi}{\frac{1}{2}\rho l d U^2}, \tag{6}$$

$$C_{Fa} = \frac{F_0(-\cos \psi)}{\frac{1}{2}\rho l d U^2}, \tag{7}$$

where ψ denotes the phase angle between force and displacement. Positive values of C_{Fv} indicate excitation, as energy flows from the fluid into the structure. Likewise, negative values of C_{Fv} indicate damping, as energy flows from the structure to the fluid. The time-averaged power flow can be shown to be a scaled product of the transverse velocity and C_{F_v} as follows:

$$\frac{1}{\tau}\int_0^\tau F(t)\dot{y}(t)dt = \frac{1}{2}F_0\omega Y_0 \sin \psi = \frac{1}{4}Y_0\omega C_{F_v}\rho l d U^2. \tag{8}$$

Note that a negative C_{F_a} indicates positive added mass.

Many of the data sets obtained show multiple spectral peaks, however, requiring an alternative method of analysis. After calculation of the spectra for a given run, we chose the lowest dominant peak frequency and divided the data into bins of five periods each. We then consolidated the multi-mode signals into *equivalent* lift and added mass coefficients which preserve the power flow of the pure sinusoidal

coefficients (Gopalkrishnan 1992). These formula also apply to the case with more than two distinct frequencies. We have

$$C_{F_v} = \sqrt{\frac{2}{\tau}} \frac{\langle F(t), \dot{y}(t) \rangle}{\sqrt{D\dot{y}(t), y(t)\rangle}} \frac{1}{\frac{1}{2}\rho l d U^2},$$

(9)

$$C_{F_a} = \sqrt{\frac{2}{\tau}} \frac{\langle F(t), \ddot{y}(t) \rangle}{\sqrt{\langle \ddot{y}(t), \ddot{y}(t)\rangle}} \frac{1}{\frac{1}{2}\rho l d U^2},$$

(10)

where τ is the integration interval. To see that the power flow has the same dependence on C_{F_v}, we make the substitutions again as in equation (8):

$$\frac{1}{\tau}\langle F(t), \dot{y}(t) \rangle = \frac{1}{\tau} C_{F_v} \frac{1}{2}\rho l d U^2 \sqrt{\frac{\tau}{2}\langle \dot{y}(t), \dot{y}(t)\rangle}.$$

(11)

In the case of single-mode input, the square root reduces to $Y_0\omega\tau/2$, and the result of equation (8) is recovered. In the case of multiple components, the square root reduces to the root-mean-square transverse velocity multiplied by $\tau/\sqrt{2}$. The lift coefficient and phase angles reported in the following sections are averaged and standard deviations of values obtained in the bins.

3. SINGLE-MODE FREE VIBRATIONS

A typical set of inertia-corrected force and position signals is given in Figure 3, for the case $\zeta = 0.01$ and $\omega_t = 1.2$. This run contains significant amplitude modulation in position, but the force signal has some higher harmonics evident, especially in the position cusps (Gopalkrishnan 1992). Employing the inner-product calculations above, the phase angle in this case is near zero degrees.

The total lift, phase, and amplitude data are shown in Figure 4, for the complete range of damping ratios $\zeta = \{0.000, 0.001, 0.010, 0.100\}$ and tunings $\omega_t = 0.40 - 1.70$. Vertical bars, where shown, indicate addition and subtraction of one standard deviation. The amplitudes given are the average of the one-tenth highest values. The
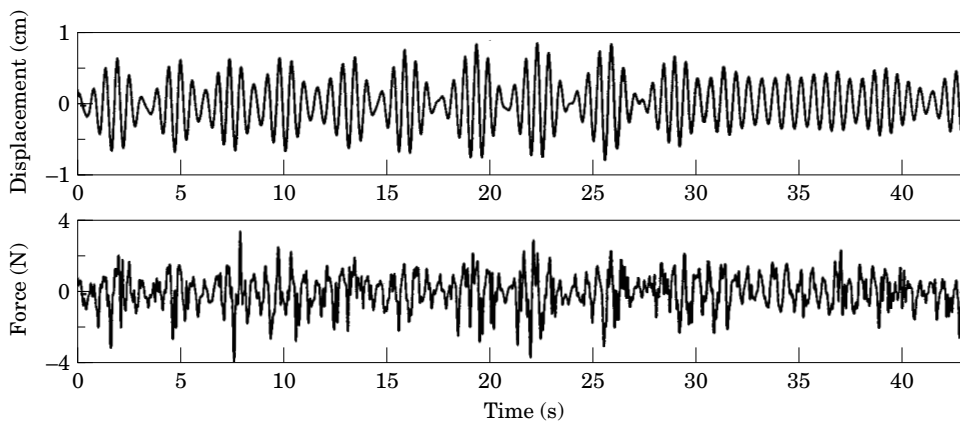

Figure 3. Typical displacement and force signals; $\omega_t = 1.2$, $\zeta = 0.01$. The position is bimodal with peaks near the structural mode and the shedding rate, while the force signal contains energy primarily at the shedding rate.
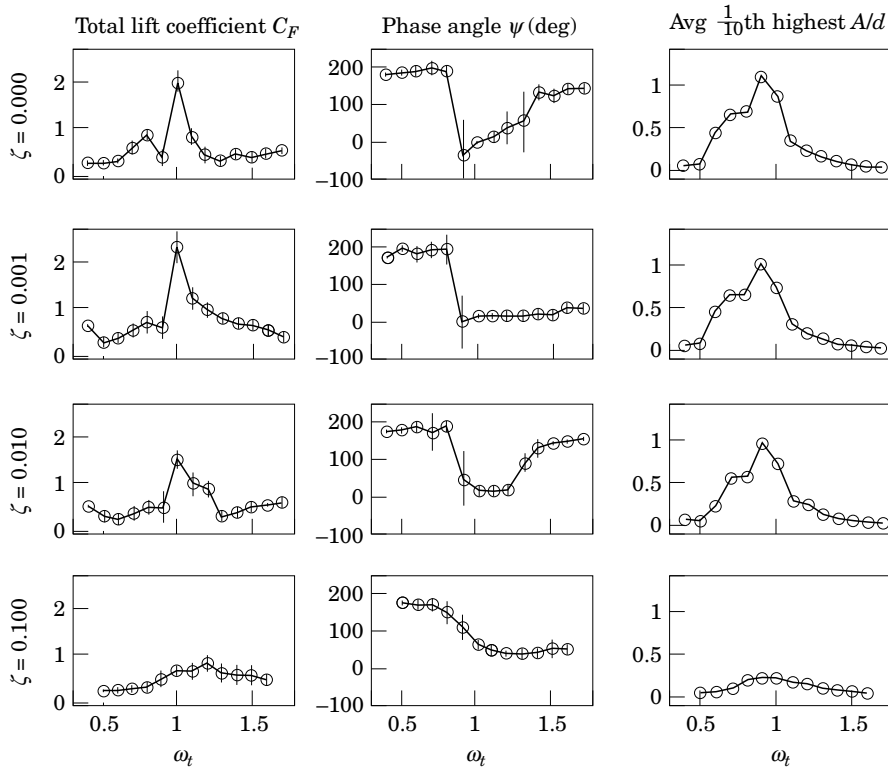
Figure 4. Total lift coefficient, nondimensional amplitude, and phase are shown for four damping ratios, as a function of structural tuning ω_t. Vertical lines indicate one standard deviation from the mean value.

peak displacement of about one diameter is achieved near $\omega_t = 0\cdot9$ in all cases, corresponding to dramatic phase angle changes and a weak local minimum in the total lift coefficient. The A/d ratios are also characterized by a step change, which is known to involve a hysteretic response to steady-stream velocity (Feng 1968; Berger 1978). The lift coefficient has maximum value at $\omega_t = 1\cdot0$, with the phase generally stabilized at this point. An interesting point is the variation of phase in the case $\zeta = 0\cdot001$, compared to the cases $\zeta = 0\cdot000$ and $\zeta = 0\cdot010$. The latter two curves share a gradual return to $\omega = 180$ deg., while the first remains near a value of zero degrees as ω_t increases. This observation suggests a polytypic dependence of phase on damping ratios. However, the amplitude ratios appear consistent; that is, they vary inversely with ζ. Much stronger A/d variations for the range $\zeta = 0\cdot0015$–$0\cdot0030$ have been found in air experiments (Gonswami *et al.* 1993).

Figures 5–7 show the amplitude and force spectra from the majority of experiments, confirming that the vibrations follow the fixed-cylinder vortex-shedding rate when the structural modal frequency exceeds it (Feng 1968; Anand 1985). On each subplot, log power spectral densities for successive cases are offset by four orders of magnitude; the position plots show the A/d p.s.d., and the force coefficient plots give the p.s.d. of the force coefficient

$$C_F = \frac{F_m + m_{cyl}\ddot{y}}{\frac{1}{2}\rho U^2 dl}. \tag{12}$$

A single horizontal dotted line for each position p.s.d. denotes the value $0\cdot0001$, or 1% of the A/d ratio. On the force subplots, the reference line indicates a force coefficient
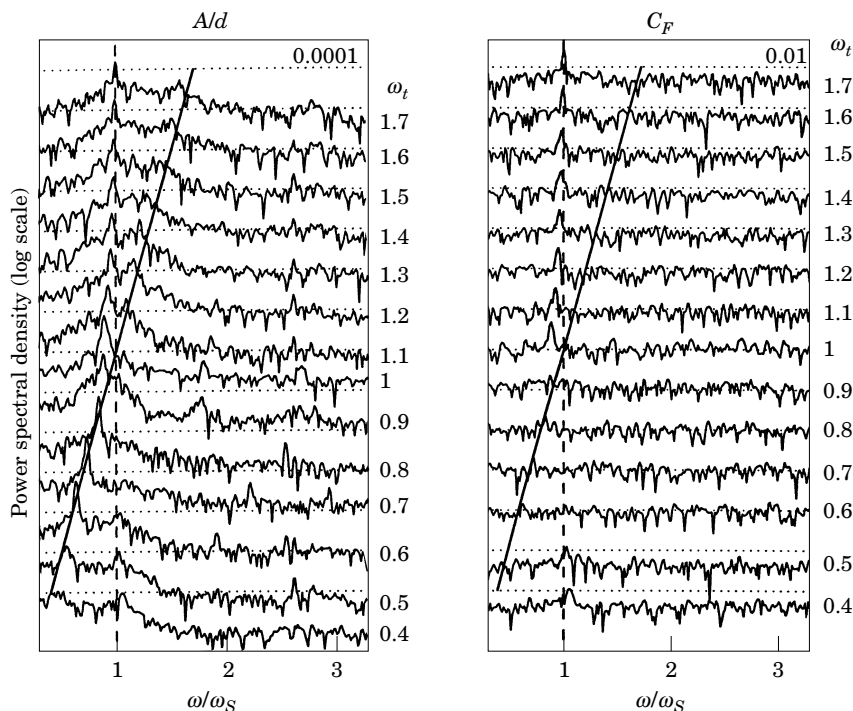
Figure 5. Amplitude and force coefficient power spectra for the single-mode model with damping ratio 0·001. The curves are offset by four orders of magnitude, with reference lines indicating $A/d = 0·01$ and $C_F = 0·1$. The dashed vertical line indicates the nominal shedding frequency, and the slanted heavy line locates the structural mode for each ω_t considered.
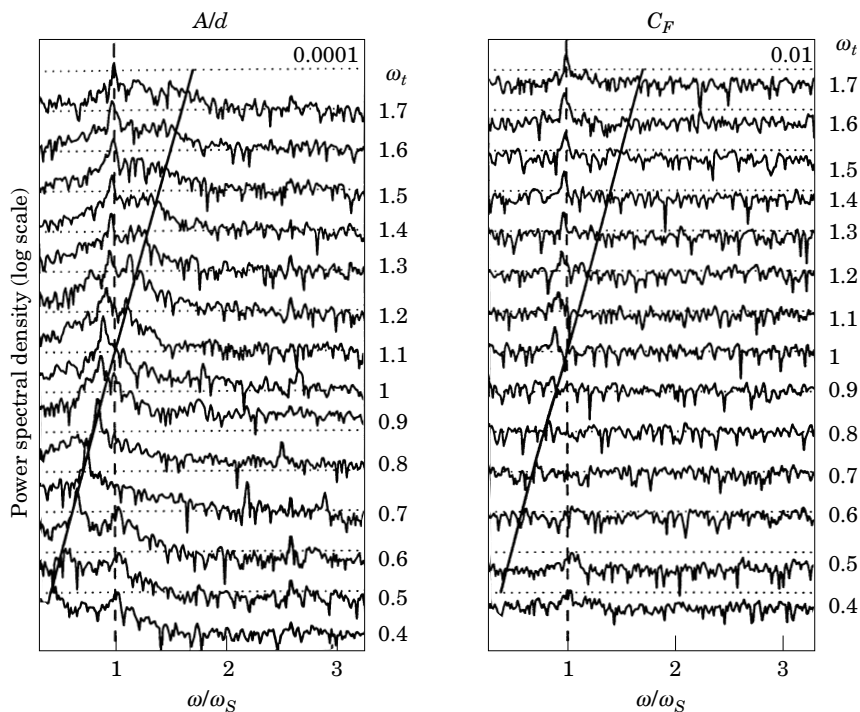

Figure 6. Amplitude and normalized force spectra for the single-mode model with damping ratio 0·010. See Figure 5 caption.
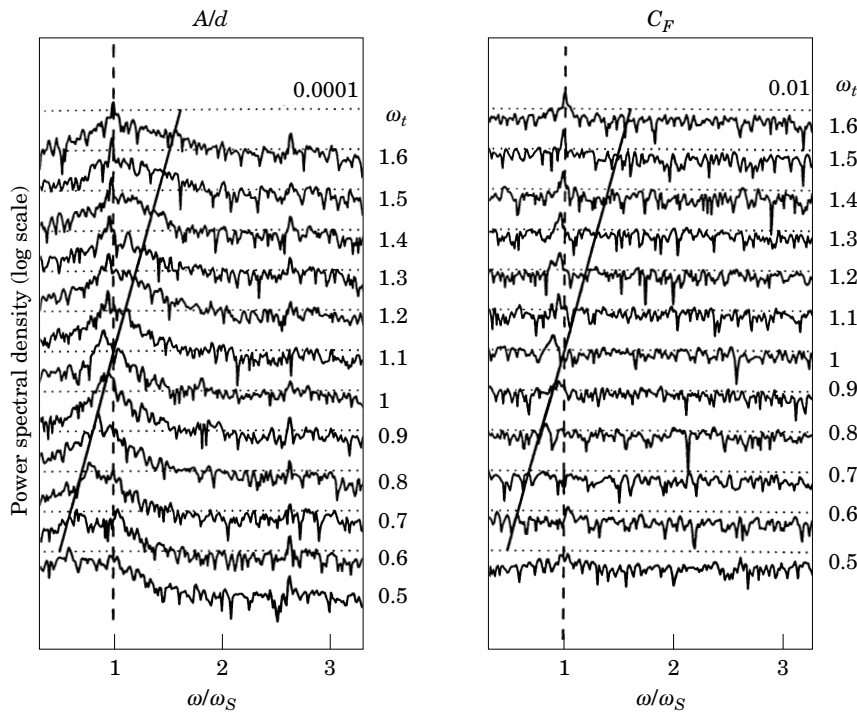
Figure 7. Amplitude and normalized force spectra for the single-mode model with damping ratio 0·100. See Figure 5 caption.

p.s.d. of 0·01, or 10% of the nominal fluid force. A heavy slanted line indicates the structural mode associated with each experiment.

For low damping, we observe narrow-band displacement peaks growing in the range $\omega_t = 0·6–1·0$. Localized beating phenomena then occurs just above the crossover ($\omega_t = 1·1 − 1·3$); beyond this point, the responses diminish and broaden mildly, as the shedding mode dominates. The low-damping displacement spectra also show some weak indication of second and third harmonics (Wu 1992), usually below $\omega_t = 1·0$. Large damping tends to create more broadband displacement spectra, especially near cross-over, with very little beating. The force signals largely comprise white noise when $0·5 < \omega_t < 1·0$, organizing to a single peak near the shedding rate, at lower and higher values. The force signals contain little evidence of beating, even when the displacement is beating strongly. Additionally, neither the force nor displacement spectra indicate clearly why phase in the three cases $\zeta = 0·000$, $0·001$ and $0·010$ should be distinct, as pointed out previously.

Figure 8 compares the new data with that of several previous studies. In the first case, we replot the amplitude ratios against the observed frequencies, for damping ratios of [0·000, 0·001, 0·010]. Additionally, zero contours of the lift coefficient in phase with velocity C_{F_v} are shown; the data are from Gopalkrishnan (1992), for forced oscillation tests with beating. Low structural damping implies nearly zero average power flow in the steady state, so at low ω_t, i.e., during lock-in, we expect the new data points to fall near these zero contours. The reduced amplitude associated with higher damping provides an additional line (not shown) which corresponds to a positive C_{F_v}.

As ω_t increases, the observed frequency conforms to the fixed-cylinder vortex-shedding rate ω_S, and the amplitude in all cases decreases. This brings the new data
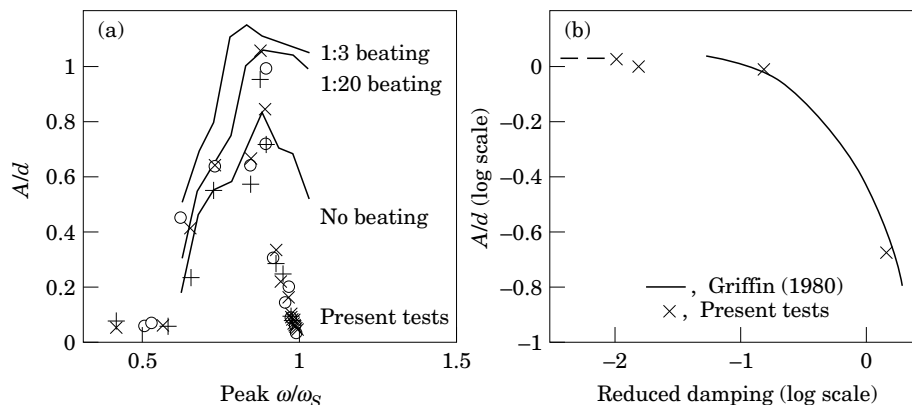
Figure 8. (a) Amplitude ratios in lightly-damped free vibration follow the zero contours of lift in phase with velocity, obtained for different forced-beating patterns by Gopalkrishnan (1992). Lift is positive below the contour lines, and the symbols are: ×, $\zeta = 0.000$; ○, $\zeta = 0.001$; +, $\zeta = 0.010$. (b) Peak amplitude ratios, for the values of ζ considered, match the average curve for data presented by Griffin (1980). The leftmost experimental point is at zero damping.

points into a positive C_{F_v} area in Gopalkrishnan's plots, and therefore, in this regime the forced- and free-vibration results are in disagreement. Specifically, the zero-power condition *must* hold in the free vibration, while a positive C_{F_v} indicates power flowing from the fluid into the cylinder. We believe that the drastic variation of phase with vibration frequency near the vortex-shedding rate [e.g., Figure 4 and Staubli 1983)] may be responsible for the discrepancy.

In the second plot of Figure 8, the peak amplitude ratio is given as a function of reduced damping, here defined by

$$k_r = \frac{8\pi^2 S^2 m \zeta}{\rho d^2}. \tag{13}$$

The data are compared against the generalized curve given by Griffin (1980), representing a considerable experimental base of data. For further comparison with other work, the mass ratio $2m/\rho d^2$ in our tests is calculated to be $11 \cdot 0$. This value is quite low with respect to air tests (>30), but fairly high with respect to typical water tests ($\geq 1 \cdot 5$). One well-known effect of a low mass ratio is that the lock-in range of reduced velocity is greatly broadened; the force spectra shown in Figure 5 generally agree with this point, as lock-in to the structural mode holds up to $V_r \simeq 8 \cdot 75$. To summarize, the single-mode free vibration data obtained using force feedback closely replicates the responses reported by other researchers.

4. THE INCLINED CABLE

4.1. BACKGROUND

Closely spaced linear vibrational modes, often manifested as beating, can occur in shallow-sag cables (Irvine & Caughey 1974; Triantafyllou 1984). The natural frequencies vary as a function of the nondimensional structural parameter λ,

$$\lambda = \sqrt{\frac{EA}{T_a}} \left(\frac{WL}{T_a} \right) \cos \phi_a, \tag{14}$$

where ϕ_a and T_a are the mean angle and top tension. Horizontal systems ($\phi_a = 0$)

experience mode cross-over, in which the odd modes transition to higher odd modes through symmetric growth of side lobes; the antisymmetric modes are not affected by λ. For inclined catenaries, the modal frequency lines do not cross, but veer apart instead. The avoided crossings can be arbitrarily close, or quite disparate, depending on the ratio EA/T_a, which relates axial to lateral wave speed. In both horizontal and inclined systems, however, dynamic tensions can be extremely high near the cross-over region, and therefore understanding the natural response at this point is of critical importance (Triantafyllou & Grinfogel 1986).

   The natural modes and planar mode shapes for a suspended cable can be computed using the formulation developed by Triantafyllou (1984). To enable the approach, we assume that the bending stiffness and structural damping are negligible; this latter condition is supported by the relative insensitivity of the amplitude response to reduced damping less than 0·10 (Griffin 1980).

4.2. IMPLEMENTATION

Galerkin projection provides a consistent way to incorporate the cable modal dynamics into the force-feedback system (Burgess & Triantafyllou 1985). The lateral deflection is written as

$$q(s, t) = \sum_{i=1}^{\infty} Q_i(t)R_i(s), \tag{15}$$

where $Q(t)$ is the temporal component of $q(s, t)$, and $R_i(s)$ is the ith eigenfunction. This expansion is then employed in the simplified transverse equation

$$M \frac{\partial^2 q}{\partial t^2} = \frac{\mathrm{d}T_0}{\mathrm{d}s} \frac{\partial q}{\partial s} + T_0 \frac{\partial^2 q}{\partial s^2} + T \frac{\mathrm{d}\phi_0}{\mathrm{d}s}, \tag{16}$$

where the quasi-static dynamic tension is

$$T = \frac{EA}{L} \int_0^L \left[\frac{1}{2} \left(\frac{\partial q}{\partial s} \right)^2 - \frac{\mathrm{d}\phi_0}{\mathrm{d}s} q(s) \right] \mathrm{d}s. \tag{17}$$

Since the quadratic term in the integral is second-order, it is neglected in the expansion. Projection onto the mode $R_m(s)$ leads to

$$I_l\ddot{\mathbf{Q}} = (I_r + I_s + I_t)\mathbf{Q}, \tag{18}$$

where

$$I_{l_{ij}} = m \int_0^L R_i R_j \, \mathrm{d}s, \tag{19}$$

$$I_{r_{ij}} = \int_0^L \frac{\mathrm{d}T_0}{\mathrm{d}s} R_i' r_j \, \mathrm{d}s, \tag{20}$$

$$I_{s_{ij}} = \int_0^L T_0 R_i'' R_j \, \mathrm{d}s, \tag{21}$$

$$I_{t_{ij}} = -\frac{EA}{L} \int_0^L R_j \left[\int_0^L \frac{\mathrm{d}\phi_0}{\mathrm{d}s} R_i \, \mathrm{d}s \right] \mathrm{d}s. \tag{22}$$

As discussed in the Introduction, fluid forcing in a full-scale deployment generally occurs along the entire cable length, and hence correlation length and boundary conditions may play a significant role. In tests with a short cylinder, the forces are measured at only *one* location on the continuous structure. In the absence of a complete hydrodynamic model for the cable, the simplest course is to zero the forcing outside the experimental cylinder. This is akin to suspending the member in air, with the test cylinder passing through a small water channel. The force input and motion output of our system is taken to be at location s_0. Using projection, the forcing term becomes

$$\int_0^L R_m(s)F(s,t)\,\mathrm{d}s \Rightarrow F(t)\int_{s_0-l/2}^{s+l/2} R_m(s)\,\mathrm{d}s. \tag{23}$$

The motion for the motor to follow is

$$q(s_0,t) = \sum_{i=1}^{\infty} Q_i(t)R_i(s_0). \tag{24}$$

The dynamic system of equation (18) may contain any number of modes, but only two are required to capture the first avoided crossing. In a manner entirely parallel to that of the single-mode case [equation (3)], the set of differential equations is assembled into matrix form, and discretized using the matrix exponential and zero-order hold. One notable difference is that where in the single-mode case, the states alone form the servomotor setpoint, the setpoint now must be computed as a linear combination of projected components, using equation (24).

Using the physical parameters in Table 1, we generated the natural frequencies shown as solid curved lines in Figure 9. The static cable shape and associated mode shapes are shown in Figure 10. The reader should note that this example has a rather deep sag. The parameters were chosen to match the size and bandwidth of the experimental apparatus, and specifically to incur closely spaced hybrid modes. In this system, the transverse mode shapes are not orthogonal near crossover, so some weak coupling occurs. Eigenvalues for the first two modes at the point of nearest approach are $\{0 \pm j10\cdot349, \quad 0 \pm j11\cdot172\}$, and the eigenvectors are $\{-0\cdot995, \quad -0\cdot030, \quad 0 \pm j0\cdot096, \quad 0 \pm j0\cdot0029\}$ and $\{0\cdot096, \quad -0\cdot991, \quad 0 \pm j0\cdot0086, \quad 0 \pm j0\cdot089\}$. The variation in the avoided crossing value of λ from the usual value of 2π is due to the significant added mass of the cable in water.

Eigenfunction zeros tend to prohibit excitation at their corresponding natural frequencies. Specifically, these near-zero values are as shown below.

Mode	λ/π	s/L
2	1·27	0·50
1	1·50	0·25
2	1·78	0·75
2	2·11	0·75

They can be seen in Figure 10. In the more specific case, projection of the two-mode system onto a small segment leads to a transfer-function zero between the poles. Proximity of this zero to the pole pair depends on both λ/π and the location along the cable s_0, as shown in Figure 11(a). At the cable center, the zero is essentially independent of λ/π, whereas in the other cases it is located nonsymmetrically. These modal zeros can prevent substantial motion from occurring, even when the shedding

TABLE 1

Physical parameters for inclined cable calculations.

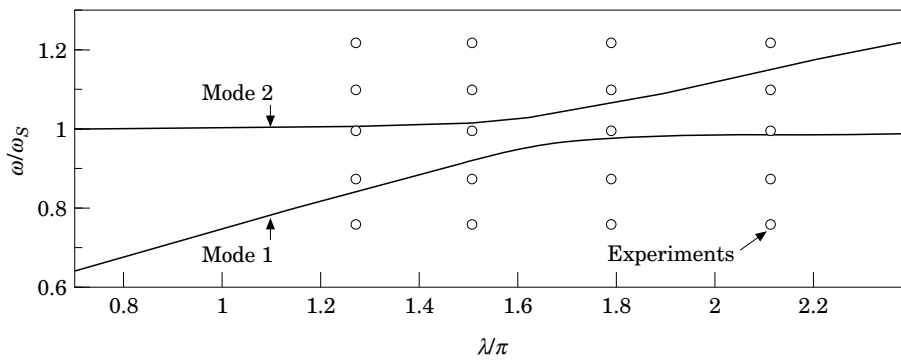| Parameter	Value	Units
Length	5·0	m
Diameter	3·17	cm
Cable density	7000	kg/m^3
Young's modulus	11–270	MPa
ϕ_a	28·28	deg
T_a	528	N

Figure 9. Cross-over avoidance for the first two natural modes (solid curved lines) is shown for the parameters of Table 1. Also shown are 20 points for the test runs; five different shedding rates for four different structures parameterized by (λ/π).

rate is very close; see the spectra in the following section. A characteristic structural natural frequency corresponds to the zero-moment value, valid for white-noise input. If $G(j\omega)$ is the system transfer function, we set

$$\omega_z = \frac{\displaystyle\int_0^\infty |G(j\omega)\omega|\,\mathrm{d}\omega}{\displaystyle\int_0^\infty |G(j\omega)|\,\mathrm{d}\omega}. \tag{25}$$
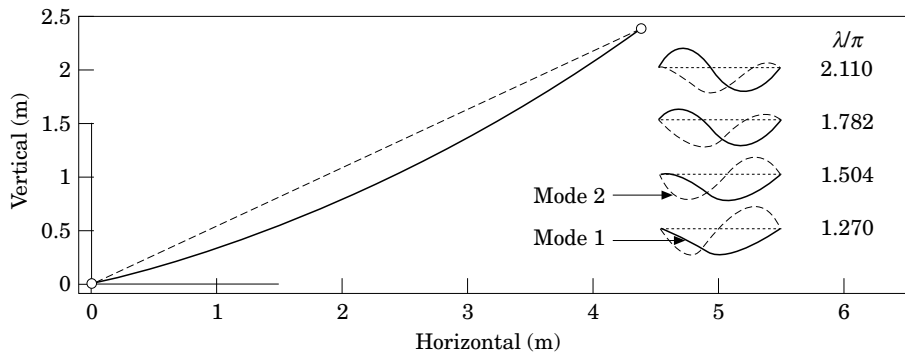

Figure 10. Coupled modes for the suspended cable are computed from linearization about the static configuration shown (Table 1). Fluid flow is perpendicular to the page.
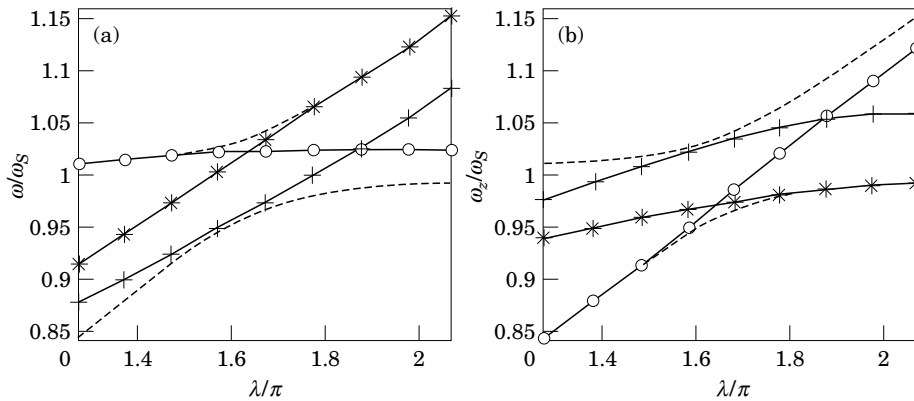
Figure 11. (a) Galerkin projection of the cable equations onto the test cylinder leads to a zero located between the natural modes. (b) The corresponding zero-moment frequencies ω_z. $---$, Natural modes; $+$, for $s/L = 0.25$; $\bigcirc$, for $s/L = 0.50$; $*$, for $s/L = 0.75$.

Figure 11(b) indicates these zero-moment frequencies, which are a spatially varying nonlinear function of the structured parameter λ/π.

4.3. EXPERIMENTAL RESULTS

We conducted 60 tests, covering four λ and five ω_S points, shown as points in Figure 9 along with the first two natural modes. For each of the 20 $\{\lambda, \omega_S\}$ points, we considered three locations on the cable: $s_0 = \{0.25L, \ 0.50L, \ 0.75L\}$. The fixed-cylinder vortex-shedding rate was varied directly by changing the towing speed; the range of 0.225 to 0.360 m/s covers all the natural modes, as shown. The presentation of data parallels that of the single-mode tests above, so that direct comparisons can be made.

The displacement and force coefficient power spectra are given in Figures 12–14. In these plots, five orders of magnitude separate the curves; otherwise, they are directly comparable to the single-mode plots. The frequency scale is nondimensionalized to a nominal vortex-shedding rate, based on the third towing speed of 0.294 m/s. It should be pointed out that where we used the term "cross-over" to denote the point $\omega_t = 1.0$ previously, in the inclined cable case, this location is less well-defined, since the structural modes themselves have a nonuniform dependence on λ.

Overall, the displacement spectra have the same character as in the single-mode case. Double- and triple-mode responses are common, comprising the structural and shedding frequencies and tempered by the zeros described above. Perhaps more clear than in the single-mode spectra, second and third harmonics are also visible. The corrected force coefficient spectra show several significant divergences from the single-mode case, however, suggesting a variance of the wake interaction with the structure. Namely, where previously the force peak organized at cross-over ($\omega_t = 1.0$) and aligned eventually with the shedding rate, now only one of the structural modes needs to exceed the shedding rate in order to narrow the force spectrum. This point is clear in Figures 12 and 13, while in Figure 14, an even stronger statement seems to hold: narrow-band force spectra can form even if *both* structural modes are below the shedding rate. This latter figure, at $U = 0.325$ m/s, also suggests that the force peak need not occur at the shedding rate, nor at the lowest of the three frequencies. Indeed, at small λ/π, the peak aligns with the upper structural mode, while at large λ/π, it tends to reside at the lower structural frequency, being below the shedding rate in both cases. These properties are in sharp contrast to the single-mode results, suggesting a significant variation in the wake-structure interaction.
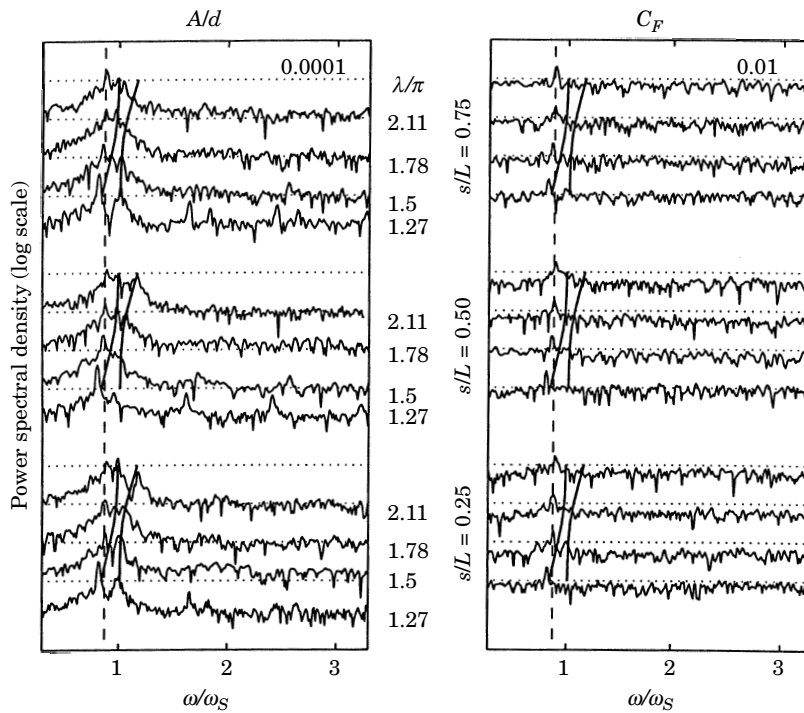
Figure 12. Log power spectra of amplitude ratio and force coefficient at $U = 0.257$ m/s. Five orders of magnitude separate the curves, and reference lines show $A/d = 0.01$ and $C_F = 0.1$. The dashed vertical line indicates the shedding rate, and the two curved solid lines indicate structural modes as the structural parameter λ/π is varied. The horizontal axis is scaled with a nominal shedding rate based on a towing speed of 0.294 m/s.

The measured force (corrected for cylinder inertia) and position signals, several of which are shown in Figures 15–17, demonstrate a variety of relations. The first example, in Figure 15, is for the second towing speed (0.257 m/s), $\lambda/\pi = 1.50$ and $s/L = 0.75$. The displacement, undergoing a changing beating pattern, has three spectral peaks: two at the structural modes, and one at the shedding rate. This triple-peak response is typical of runs at the lower two towing speeds, where the displacements tend to be small, and the structural modes exceed the shedding rate. The force signal in this run is narrow-band at the shedding rate, with no sign of beating. Figure 16 is for the middle towing speed (0.294 m/s), with $\lambda/\pi = 2.11$ and $s/L = 0.50$. Here, the amplitude-modulated displacement, with two spectral peaks, appears to be stable, and the force has similar modulation with a well-correlated envelope. However, the force spectrum shows little evidence of this envelope. In Figure 17, the displacement again has a reasonably stable amplitude modulation, but the force signal is quite disorganized, showing periods of both reduced and increased frequency. This run was at the fourth speed (0.325 m/s), and had $\lambda/\pi = 1.50$ and $s/L = 0.75$. In the single-node experiments, we see no cases in which broadband forcing leads to bimodal displacement oscillation.

The lift coefficients, phases, and amplitude ratios from the test data, shown in Figure 18, bear a strong qualitative similarity to those of the single-mode system in Figure 4. This correlation is in large part due to our use of the zero-moment frequency ω_z in the parameterization; here $\omega_t = \omega_z/\omega_S$. The large standard deviations shown, and the scatter in the mean values, are likely due to the increased spectral richness in the
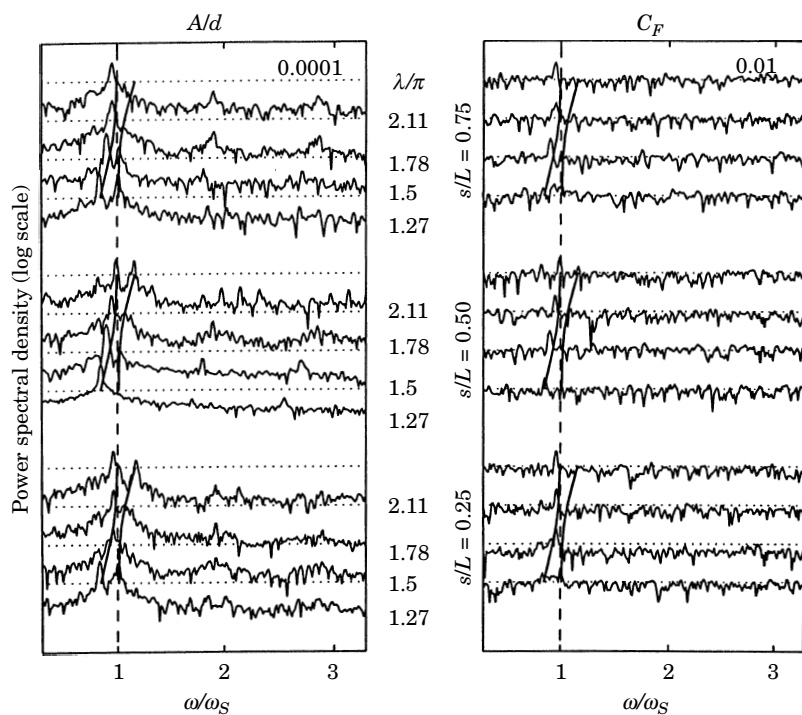
Figure 13. Log power spectra of amplitude ratio and force coefficient, at $U = 0.294$ m/s. See Figure 12 caption.
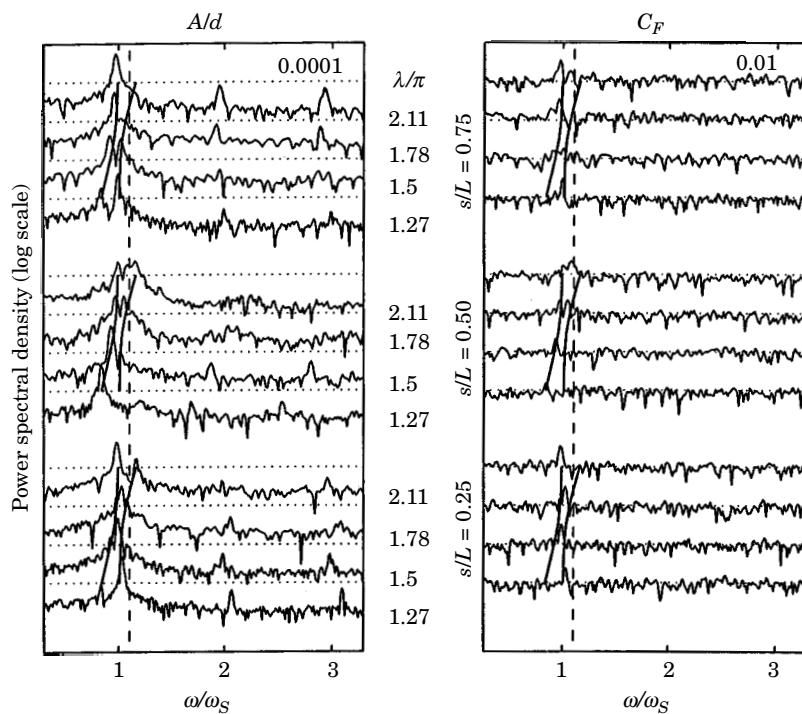

Figure 14. Log power spectra of amplitude ratio and force coefficient, at $U = 0.325$ m/s. See Figure 12 caption.
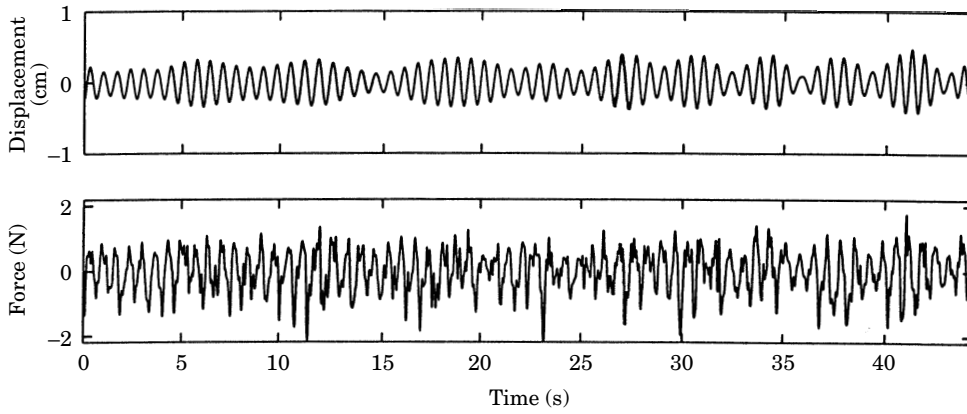
Figure 15. Amplitude and force signals for $U = 0.257$ m/s, $\lambda/\pi = 1.50$ and $s/L = 0.75$. Evidence of three peaks in the displacement spectra lead to a varying modulation, while forcing is primarily at the shedding rate.
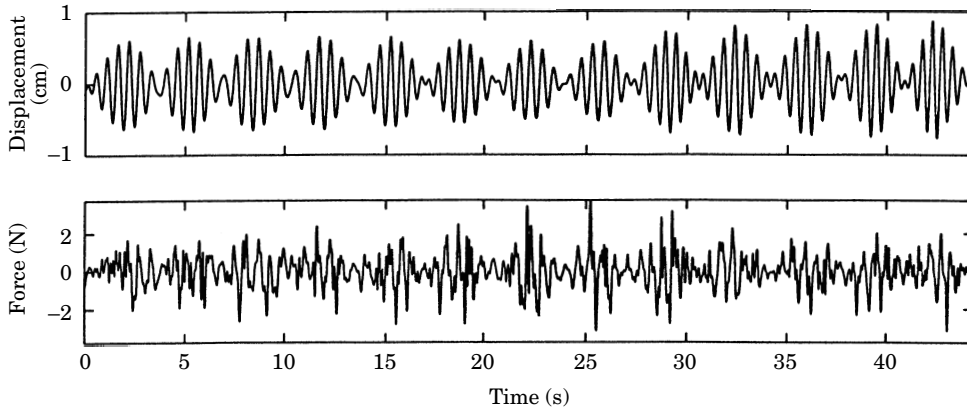

Figure 16. Amplitude and force signals for $U = 0.294$ m/s, $\lambda/\pi = 2.11$ and $s/L = 0.50$. The position spectra are strongly bimodal, and the force signal shows some associated modulation.
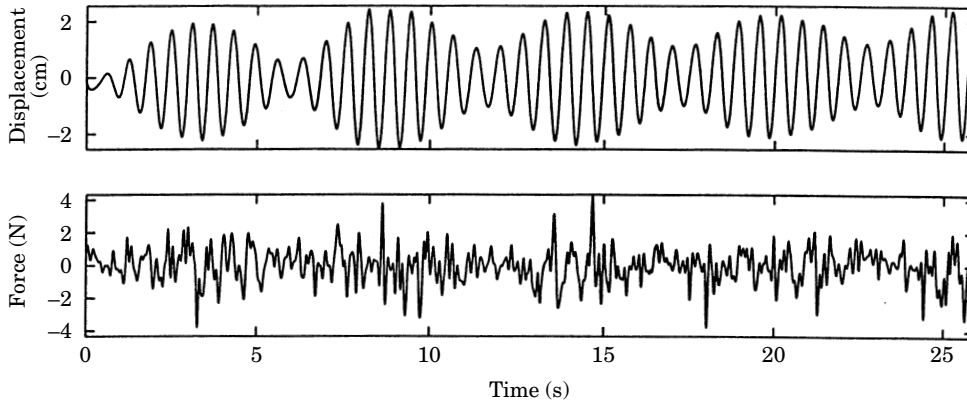

Figure 17. Amplitude and force signals for $U = 0325$ m/s, $\lambda/\pi = 1.50$ and $s/L = 0.75$. The cylinder oscillates at the two structural modes, but the force is broadband, with the structural modes well below the shedding rate.
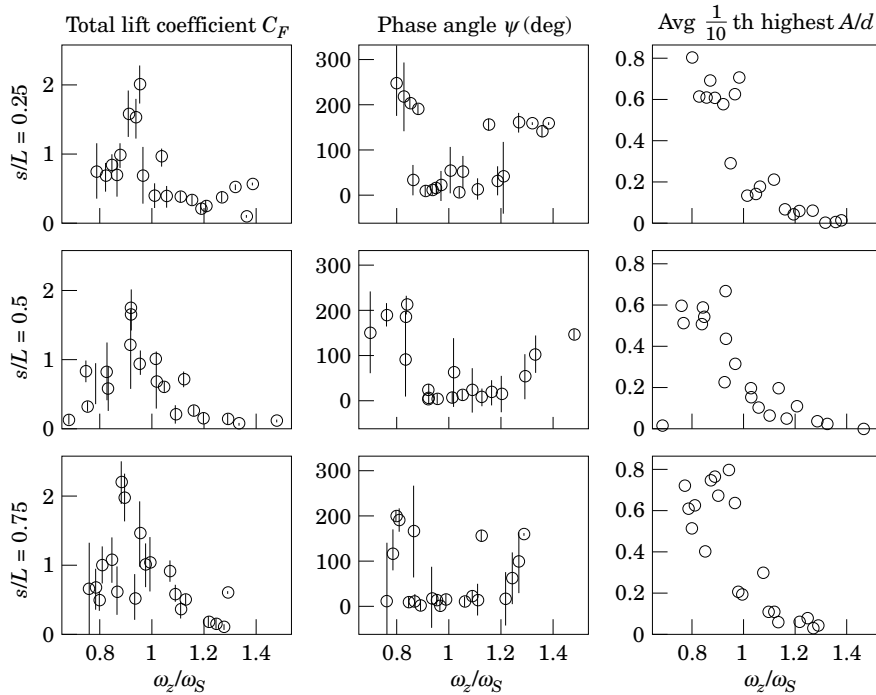
Figure 18. Lift coefficient, phase, and amplitude ratios for the inclined cable experiments. Overall, most of the character of Figure 4 is recovered, when the zero-moment frequency scaling is used.

responses, since the inner-product calculation exactly describes only monochromatic processes. The force coefficients reach peak values of approximately two, peaking in the range $\omega_t = 0 \cdot 9 - 1 \cdot 0$. Additionally, the phase has a zero-angle regime in the range $\omega_t = 0 \cdot 9 - 1 \cdot 25$; both of these quantities are in good agreement with the single-mode results. Amplitude ratios are somewhat reduced, however, and show a large amount of scatter. The hysteretic step has apparently vanished as well, although admittedly the lower limit of ω_t is not as low as in the single-mode tests. Only one point, for $s/L = 0 \cdot 50$ and $\omega_t = 0 \cdot 66$, indicates that the subcritical tuning point has been passed.

5. CONCLUSIONS

Accurate laboratory testing of fluid interaction with complex, compliant structures requires scaled hardware, or a short-span hybrid approach which employs real-time simulation. The force-feedback scheme described in this paper can address a range of free-vibration models, including multiple modes, traveling waves (through finite-difference discretization), and nonlinearities. Application to real engineering problems, however, may require the use of hydrodynamic models outside the test cylinder.

In single-mode experiments, we found good agreement with the work of other researchers, in lift coefficient, phase, and peak amplitudes. Force spectra for the low-damping tests are generally broadband in the lock-in regime, and narrowband outside, while the cylinder displacement undergoes significant amplitude modulation near the lock-in cross-over point.

Dynamic responses for multi-mode models, arising from inclined cable dynamics, can be compared to those of single-mode compliant structures with proper frequency scaling. This scaling accounts for structural zeros which are absent in most single-mode

systems. Although the observed lift, phase, and amplitude properties are similar in both single- and multi-mode cases, the spectra in the latter are more complex. Notably, only one structural mode, and sometimes neither, needs to exceed the fixed-cylinder vortex-shedding rate in order for the force spectrum to be narrowband. This fact is in contrast to single-mode results ($\omega_t > 1 \cdot 0$), and suggests that the presence of two structural modes provides to the wake a new mechanism for organizing. Flow-visualization tests are anticipated which will help to describe this interaction more completely.

ACKNOWLEDGMENTS

REFERENCES

ALEXANDER, C. M. 1981 The complex vibrations and implied drag of a long oceanographic wire in cross-flow. *Ocean Engineering* **8,** 379–406.

ANAND, N. M. 1985 Free-span vibration of submarine pipelines in steady and wave flows. Dr. Eng. Thesis, Norwegian Institute of Technology, Trondheim, Norway.

BERGER, E. 1978 Some new aspects in fluid oscillator model theory. In *Proceedings 3rd Colloquium on Industrial Aerodynamics,* Aachen, Germany.

BISHOP, R. E. D. & HASSAN, A. Y. 1964 The lift and drag forces on a circular cylinder oscillating in a flowing fluid. *Proceedings of the Royal Society of London* **A277,** 51–75.

BURGESS, J. J. & TRIANTAFYLLOU, M. S. 1985 Time-domain simulation of the dynamics of ocean towing lines. In *Proceedings 3rd International Symposium on Practical Design of Ships and Mobile Units,* Trondheim, Norway.

EVERY, M. J., KING, R. & GRIFFIN, O. M. 1981 Hydrodynamic loads on flexible marine structures due to vortex shedding. In *Proceedings ASME Winter Annual Meeting,* Washington, D.C., U.S.A.

FENG, C. C. 1968 The measurement of vortex-induced effects in flow past stationary and oscillating circular and D-section cylinders. Master's Thesis, University of British Columbia, Victoria, British Columbia, Canada.

GONSWAMI, I., SCANLAN, R. H. & JONES, N. P. 1993 Vortex-induced vibration of circular cylinders. I: Experimental data. *ASCE Journal of Engineering Mechanics* **119,** 2270–2287.

GOPALKRISHNAN, R. 1992 Vortex-induced forces on oscillating bluff cylinders. Ph.D. Thesis, Massachusetts Institute of Technology, Cambridge, Massachusetts, U.S.A.

GRIFFIN, O. M. 1980 Vortex-excited cross-flow vibrations of a single cylindrical tube. *ASME Journal of Pressure Vessel Technology* **102,** 158–166.

GROSENBAUGH, M. A., YOERGER, D. R., HOVER, F. S. & TRIANTAFYLLOU, M. S. 1991 Drag forces and flow-induced vibrations of a long vertical tow cable—Part II: Unsteady towing conditions. *ASME Journal of Offshore Mechanics and Arctic Engineering* **113,** 199–204.

HOWELL, C. T. 1989 Dynamics of cable subjected to shear current excitation. Master's Thesis, Massachusetts Institute of Technology, Cambridge, Massachusetts, U.S.A.

IRVINE, H. M. & CAUGHEY, T. K. 1974 The linear theory of free vibrations of a suspended cable. *Proceedings of the Royal Society of London* **A341,** 299–315.

MASON, M. T. 1981 Compliance and force control for computer-controlled manipulators. *IEEE Transactions of Systems, Man, and Cybernetics* **11,** 418–432.

MERCIER, J. A. 1973 Large amplitude oscillations of a circular cylinder in a low-speed stream. Ph.D. Thesis, Stevens Institute of Technology, Hoboken, New Jersey, U.S.A.

MOE, G. & WU, Z.-J. 1989 The lift force on a vibrating cylinder in a current. In *Proceedings 8th International Conference on Offshore Mechanics and Arctic Engineering,* The Hague, Netherlands.

NAKANO, M. & ROCKWELL, D. 1993 The wake from a cylinder subjected to amplitude-modulated excitation. *Journal of Fluid Mechanics* **247,** 79–110.

PROTOS, A., GOLDSCHMIDT, V. W. & TOEBES, G. H. 1968 Hydroelastic forces on bluff cylinders. *ASME Journal of Basic Engineering,* **35,** 378–386.

SARPKAYA, T. 1978 Fluid forces on oscillating cylinders. *ASCE Journal of Waterway, Port, Coastal, and Ocean Division,* **104,** 275–290.

SARPKAYA, T. 1979 Vortex-induced oscillations: a selective review. *Journal of Applied Mechanics* **46,** 241–258.

SCHARGEL, R. S. 1980 The drag coefficient for a randomly oscillating cylinder in a uniform flow. Master's Thesis, Massachusetts Institute of Technology, Cambridge, Massachusetts, U.S.A.

STANSBY, P. K. 1976 The locking-on of vortex shedding due to the cross-stream vibration of circular cylinder in uniform and shear flows. *Journal of Fluid Mechanics* **77,** 641–665.

STAUBLI, T. 1983 Calculation of the vibration of an elastically-mounted cylinder using experimental data from forced oscillation. *ASME Journal of Fluids Engineering* **105,** 225–229.

TRIANTAFYLLOU, M. S. 1984 The dynamics of taut inclined cables. *Quarterly Journal of Mechanics and Applied Mathematics* **37,** 421–440.

TRIANTAFYLLOU, M. S. & GRINFOGEL, L. 1986 Natural frequencies and modes of inclined cables. *Journal of Structural Engineering* **112,** 139–148.

VANDIVER, J. K. & CHUNG, T. Y. 1987 Hydrodynamic damping of flexible cylinders in sheared flow. in *Proceedings Offshore Technology Conference,* Houston, Texas, U.S.A., 343–353.

WU, Z.-J. 1992 Higher frequency hydrodynamic force components on a vibrating cylinder in current. In *Proceedings International Offshore and Polar Engineering Conference,* San Francisco, California, U.S.A., 375–382.

YOERGER, D. R., GROSENBAUGH, M. A., TRIANTAFYLLOU, M. S. & BURGESS, J. J. 1991 Drag forces and flow-induced vibrations of a long vertical tow cable—Part I: Steady-state towing conditions. *ASME Journal of Offshore Mechanics and Arctic Engineering* **113,** 30–36.

APPENDIX: NOMENCLATURE

$y(t)$, Y_0	lateral deflection of test cylinder, single-mode peak value
$F(t)$, $F_m(t)$	fluid-only, measured force on test cylinder
m_{cyl}	material mass of test cylinder
l, d	cylinder length, diameter
U	towing speed
ρ	fluid density
S, ω_S	Strouhal number, fixed-cylinder vortex-shedding frequency
m, b, k, ζ	mass, damping, stiffness, and damping ratio of single-mode system
ω_d	structural damped frequency
F_0, ψ	lift force amplitude, phase
C_F, C_{Fv}, C_{Fa}	force coefficient: total, in phase with velocity, acceleration
k_r	reduced damping
L	cable length
A	cable cross-sectional area
W	cable weight per unit length in water
M	effective lateral mass per unit length
E	Young's modulus of cable
ϕ_a	mean angle of inclination
T_a	projection of top tension along ϕ_a
λ	structural parameter for suspended cables
$\omega_z(\lambda)$	zero-moment frequency
s	cable axial coordinate
$q(s, t)$	cable lateral deflection
$\phi_0(s)$, $\phi(s, t)$	static, dynamic cable angle
$T_0(s)$, $T(s, t)$	static, dynamic cable tension
$Q_i(t)$, $R_i(s)$	temporal, spatial components of $q(s, t)$
s_0	test cylinder location on cable